

Reconstructing Stellar DEMs from X-ray Spectra

CHASC (California-Harvard AstroStatistics Collaboration)

www.ics.uci.edu/~dvd/astrostat.html

Hosung Kang (kang@stat.harvard.edu, Department of Statistics, Harvard University),

David A. van Dyk (Department of Statistics, University of California at Irvine),

Vinay L. Kashyap (Harvard-Smithsonian Center for Astrophysics), and Alanna Connors (Eureka Scientific).

Abstract

The Emission Measure is a powerful tool to characterize and understand the composition and physical structure of stellar coronae. Numerous methods have been proposed in the literature to compute the Differential Emission Measure (DEM) based on line fluxes measured from identifiable lines in high-resolution EUV and X-ray spectra. **Here we describe a new and powerful method that we have developed to reconstruct DEMs that improves significantly on previous algorithms and further allows for incorporating atomic data errors into the calculations.** Some notable features of our algorithm are:

- To fit to either a selected subset of lines with measured fluxes or to perform a global fit to all lines over the full wavelength range of the instrument, to fully incorporate line blends,
- To obtain error bars to determine the significance of features seen in the reconstructed DEM,
- To directly incorporate prior information such as atomic line sequences, known atomic data errors, systematic effects due to calibration uncertainties.

We use highly structured models to account for the mixing of continuum photons with those from the multitude of spectral lines, instrumental response, the effective area of the instrument, and background contamination. We introduce the statistical framework of **data augmentation**, in which we treat photon count in each level of the hierarchical structure as missing data. We implement a multi-scale prior distribution to smooth the DEM. We also provide several DEM reconstruction results of the active star alpha Aur (Capella).

Differential Emission Measure

Definition: Distribution of the amount of material in coronae as a function of temperature. DEM summarizes the structure of coronae of stars and provides a powerful tool for understanding the energetics in stellar atmospheres.

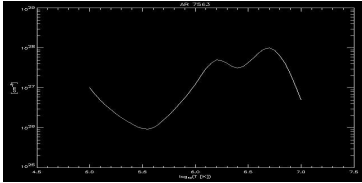


Figure 1: The Solar DEM in an Active Region. The DEM is plotted as a function of plasma temperature. Note the double peaked structure, showing evidence for material at high temperatures.

Data

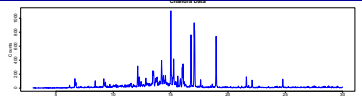


Figure 2: Chandra HRC-S/LETG spectrum of Capella (ObsID 1248). Prominent lines from O, Ne, and Fe are clearly visible. We derive an emission measure distribution that produces this spectrum.

Spectral Model

Spectral Model: We model the observed counts at energy bin i , Y_i^{obs} , as independent Poisson variables with intensity

$$\xi_i = \sum_{j=1}^J M_{ij} d_j (\lambda_j^c + \sum_{l \in \text{energy bin } j} \lambda_l^l) + \lambda_i^b, \quad i \in \{1, \dots, I\}$$

- the $I \times J$ matrix $M = \{M_{ij}\}$ represents the **RMF**, and $\mathbf{d} = \{d_1, \dots, d_J\}$ represents the **ARF**,
- λ_i^b are the intensities due to the **background**,
- λ_j^c and λ_j^l are the continuum and line intensities, and are derived from a redistribution of the atomic emissivities across temperature, weighted by the DEM:

$$\lambda_j = \sum_{i=1}^{N_T} \Lambda_{ji} \delta_i$$

where Λ_{ji} are the emissivity matrix values and δ_i is the values of the DEM at temperature i .

Emissivity Matrix

Line and Continuum Emissivity Matrix: We use the **line emissivities** from ATOMDB v1.3 and **continuum emissivities** obtained with **PINToALE**. Each row of the emissivity matrix corresponds to a line transition (or a wavelength bin in the case of continuum); each column corresponds to the emissivity at a given temperature.

Hierarchical Missing Data Structuring

Given the DEM on a discretized temperature space, we can easily compute the fluxes from continuum and emission lines at each energy bin. Inversely given the set of conditional distributions and the the observed marginal distribution of X-ray energies, we aim to reconstruct the marginal distribution of the temperature of the corona, i.e., DEM, via **Data Augmentation**.

The model has multiple components (e.g., background, continuum and emission lines) and complex structure due to large dimensional matrices. Data augmentation methods such as the **EM** (Dempster et al.) or **DA algorithm** (Tanner and Wong) make model-fitting simpler especially in highly structured models. Thus, we impute the missing data at each level, treat them as if they were observed, and find the conditional posterior distribution of the next level missing data given the current level. This will eventually lead us to imputing the **photon counts emitted from each temperature**, where we treat the emissivity matrix as a RMF-like “response matrix” and trace the energy bin counts to the unobserved photon counts in a number of temperature bins. This makes the estimation of DEM straightforward.

Multi-Scale Smoothing

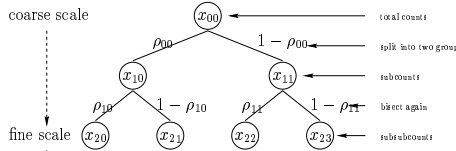


Figure 3: Multi-scale analysis and modeling represented on binary tree graph. The Poisson intensity of a “parent” node is a sum of the Poisson intensity of the two “child” nodes. The smoothness of the intensities is controlled by the splitting factors $\{\rho_{r,k}\}$. The closer $\{\rho_{r,k}\}$ is to 0.5, the heavier smoothing gets. **Prior:** $\rho_{jk} \sim \text{Beta}(\rho_{jk}|\alpha, \alpha)$. We use $\alpha = 20$ for moderate smoothing.

Simulation Study - DEM

We assume a nominal form for the DEM, generate fluxes for a set of non-standard abundances, and reconstruct the DEM from the spectrum binned over the Chandra wavelength range. Energy Range = (3, 30) Å. Number of Energy Bins = 2,161. Bin Width = 0.0125 Å, Number of Emission Lines = 10,589.

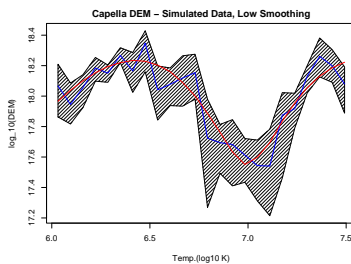


Figure 4: Error Bars for the Fitted DEMs from the Simulation Study. The blue line is the **posterior mean of the DEM** and the red line is the **true DEM** under low smoothing ($\alpha = 10$); and the shaded area represents componentwise 95% posterior intervals for the DEM.

Simulation Study - Abundance

Element	Input	Measured	95% Interval	Element	Input	Measured	95% Interval
C	0.8	0.77	(0.70, 0.84)	Si	0.8	0.80	(0.74, 0.87)
N	2	2.00	(1.92, 2.10)	S	0.8	0.93	(0.75, 1.11)
O	0.5	0.50	(0.48, 0.52)	Ar	2.8	2.90	(2.68, 3.12)
Ne	5	5.06	(4.90, 5.22)	Ca	3.8	3.82	(3.45, 4.23)
Mg	3	2.99	(2.86, 3.12)	Fe	2	2.01	(1.95, 2.08)
Al	2.5	2.37	(1.57, 3.17)	Ni	2	2.03	(1.82, 2.26)

Table 1: Posterior Mean and the 95% posterior interval for element abundance. Note that all the interval contain the input abundance which we used for data generation.

Dealing with Real Data

Due to atomic data errors and calibration errors, the theoretical and observed locations of strong lines often do not match. We allow the most influential lines to shift in position in order to obtain a better fit to the data.” Given the imputed photon counts from the lines at energy bins, we fit the center of the Lorentzian (or Gaussian) line spread function.

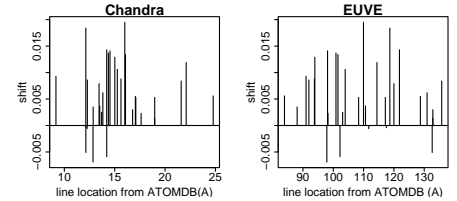


Figure 5: Line position shift (fitted-theoretical) for strong emission lines in the data range of interest.

CAPELLA DEM

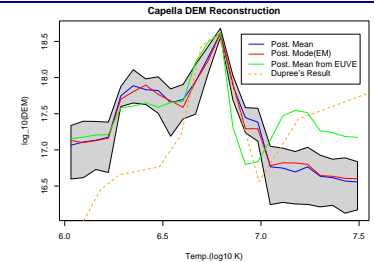


Figure 6: **Capella DEM derived from Chandra HRC-S/LETG data (see Figure 2)** Error Bars for the Fitted DEMs from Chandra data. The blue line is the **posterior mean of the DEM**, the red line is the **posterior mode of the DEM**. The shaded area represents componentwise 95% posterior intervals for the DEM. The **posterior mode of the DEM** derived from an earlier observation of Capella with the EUVE is also over-plotted (green line). The **DEM reconstructed for the EUVE observation by Dupree et al (1993)** is shown as the orange line. The features in the DEM are by and large consistent, though our reconstruction shows a significantly larger emission measure below $\log T = 6.5$.

Element	Chandra (3-30Å)			EUVE (80-140Å)		
	abundance	no. lines	Measured 95% Intvl	no. lines	Measured	95% Intvl
C	25	0.18	(0.10, 0.26)	14	0.48	(0.02, 1.59)
N	306	0.38	(0.34, 0.43)	51	0.83	(0.04, 2.43)
O	500	0.18	(0.16, 0.19)	66	0.04	(0.00, 0.12)
Ne	381	0.40	(0.38, 0.43)	376	0.83	(0.61, 1.15)
Mg	279	0.74	(0.69, 0.80)	390	0.70	(0.23, 1.30)
Al	99	0.43	(0.07, 0.82)	23	28.93	(0.91, 100.17)
Si	345	0.89	(0.81, 0.97)	100	0.72	(0.03, 2.08)
S	300	0.37	(0.18, 0.58)	58	3.29	(0.98, 5.96)
Ar	369	0.10	(0.02, 0.20)	8	NA	NA
Ca	374	0.32	(0.19, 0.46)	29	0.53	(0.01, 1.75)
Fe	5779	0.58	(0.56, 0.61)	3270	0.88	(0.73, 0.99)
Ni	1832	0.88	(0.79, 0.98)	319	0.25	(0.03, 0.56)

Table 2: Posterior Mean and the 95% posterior interval for element abundance. The abundances listed are relative to solar photospheric abundances from Anders and Grevesse (1998). Note that some elements have very few lines, therefore their posterior intervals have very wide range because of lack of information.